AOCS Performance and Stability Validation for a 160-m Solar Sail with Control-Structure Interactions

Stephanie Thomas* and Michael Paluszek†
Princeton Satellite Systems, Princeton, NJ 08542

Bong Wie‡
Arizona State University, Tempe, AZ 85287

David Murphy§
ATK Space Systems, Goleta, CA 93117

Future solar sail missions, such as NASA's Solar Polar Imager Vision, will require sails with dimensions on the order of 50-500 m. We are examining a square sail design with moving mass (trim control mass, TCM) and quadrant rotation primary actuators plus pulsed plasma thrusters (PPTs) at the mast tips for backup attitude control. Quadrant rotation is achieved via roll stabilizer bars (RSB) at the mast tips. At these sizes, given the gossamer nature of the sail supporting structures, flexible modes may be low enough to interact with the control system, especially as these actuators are located on the flexible structure itself and not on the rigid core. This paper develops a practical analysis of the flexible interactions using state-space systems and modal data from finite element models of the system. Torsion and bending of the masts during maneuvers could significantly affect the function of the actuators while activation of the membrane modes could adversely affect the thrust vector direction and magnitude. Analysis of the RSB and TCM dynamics for developing high-fidelity simulations is included.

For control analysis of the flexible system, standard finite-element models of the flexible sail body are loaded and the modal data is used to create a modal coordinate state-space system. Key parameters include which modes to include, which nodes are of interest for force inputs and displacement outputs, connecting nodes through which external forces and torques are applied from the flex body to the core, any nominal momentum in the system, and any steady rates. The system is linearized about the nominal attitude and rate. The state-space plant can then be analyzed with a state-space controller, and Bode, Nyquist, step and impulse responses generated. The approach is general for any rigid core with a flexible appendage. This paper develops a compensator for a simple two-mass flex system and extrapolates the results to the solar sail. A finite element model of the 20 m solar sail by ATK Space Systems, recently validated in ground tests, is used to demonstrate the sail analysis approach.

I. Introduction

The sail in question is a square sail with four gossamer masts and four triangular sail membranes suspended between them. Trim control masses move along the masts via lanyard lines and stepper motors, providing a center-of-mass/center-of-pressure offset which is used for pitch and yaw control. Stabilizer bars, which connect the membrane corners to the mast tips, can be simultaneously rotated to create a windmill torque for roll control. The coordinate frame of the sail - shown in a sun-synchronous Earth orbit - is given in Figure 1 on the following page.

The dawn-dusk sun-synchronous (DDSS) orbit is a possibility for a LEO sail validation mission. A sail for this mission would likely be on the order of 40 m and would require a controller fast enough to handle the solar pressure disturbances. Solar Polar Imager is an example science mission at 0.48 AU and 75°inclination, requiring a 160 m sail to achieve the science orbit in about 5-6 years. A sample maneuver from this mission

*Senior Technical Staff, 33 Witherspoon St., sjthomas@psatellite.com, (609) 279-9606. Member AIAA.
†President, 33 Witherspoon St., map@psatellite.com, (609) 279-9606. Member AIAA.
‡Professor, Dept. of Mechanical & Aerospace Engineering, bong.wie@asu.edu, (480) 965-8674. Associate Fellow AIAA.
§Chief Research Engineer, 600 Pine Ave., Dave.Murphy@atk.com, (805) 690-2439. Member AIAA.

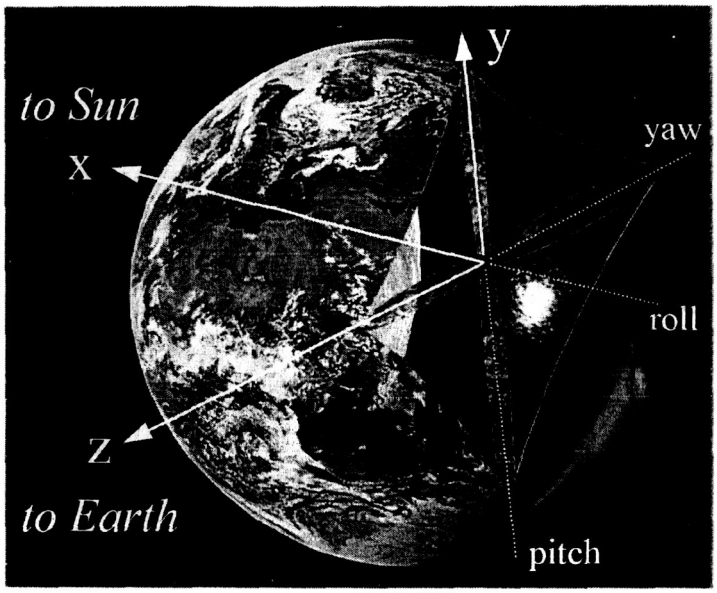

Figure 1. Sail Coordinate System

is a 3 hour, 70°rotation during the inclination cranking phase; this maneuver happens twice per orbit. In this orbit a very low control bandwidth of 0.002 rad/s is used.[5]

The software used to develop this paper is part of the Solar Sail Control Toolbox (SSCT), a MATLAB-based toolbox for analyzing and simulating sailcraft control systems.[4] The package is built around Princeton Satellite Systems standard CAD package and disturbance models, with specialized dynamics models as needed. Attitude models include a two-body gimbaled boom model and two moving mass models - one with multibody dynamics and one assuming stepper motors are the actuator. Sail models include a flat plate, a sphere, and a square sail with multiple actuators. Analysis demos are included which study the use of moving masses and roll stabilizer bars in detail. Simulations include near-Earth validation orbits and heliocentric missions such as Solar Polar Imager. The modular nature of this toolbox allows users to study various aspects of the sailcraft control problem, from orbit maneuvers to attitude control validation. The toolbox facilitates both simplified, first-level analyses of control concepts and high-fidelity simulation with full ephemeris and gravity models and numerical disturbance analysis including planetary albedo and combined thermal/optical models of the solar radiation pressure force. Third-party tools, such as structural analysis and trajectory optimization routines, can be incorporated into SSCT-based analyses since all source code is provided and simulations are script-based. Since MATLAB scripts are flexible, a single CAD model can serve as a database for both PSS simulation data and third-party tool inputs.

II. Roll Stabilizer Bar Analysis

Initial analysis of the roll bars assumed that they produce a simple windmill torque. However, high fidelity simulations of a full CAD model with disturbances in SSCT have indicated significant coupling of the yaw and pitch axes during roll stabilizer bar (RSB) actuation. An analysis of the complete geometry, for any sun vector to the sail, reveals the source of the coupling to be related to the projected area differences between the sail quadrants, which must be compensated for by the other actuators.

For the solar sail, the nominal location of the sun vector in the body frame is the $+x$ axis. In general there will be azimuth and elevation angles α and β between the sun vector and $+x$ due to thrust vector control commands or pointing errors. The sun unit vector is then expressed as:

$$\hat{u}_{sun} = \begin{bmatrix} \cos\alpha\cos\beta \\ \sin\alpha\cos\beta \\ \sin\beta \end{bmatrix}$$

Each sail quadrant can be twisted about its tack line using the RSBs. The geometry is shown in Figure 2. The sail quadrants are in the Y/Z plane, with the masts along the Y and Z axes. The four stabilizer bars are always rotated the same angle δ.

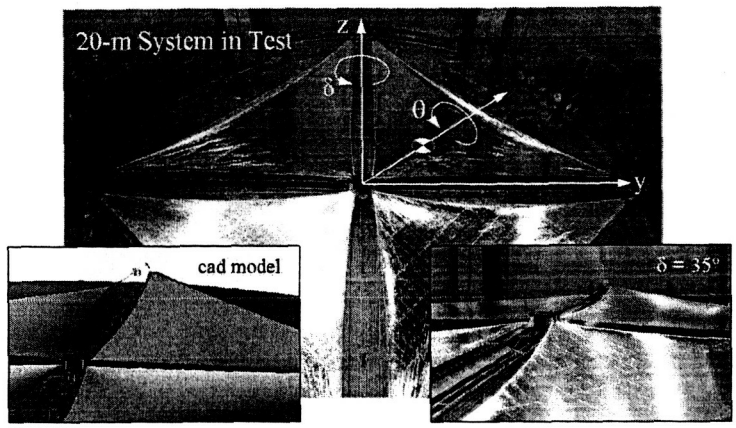

Figure 2. RSB Geometry

The centroid of a triangle is the average of the vectors to its corners. Expressed in the body frame, the sail centroid vectors are

$$\vec{r}_{cm} = \frac{l_{mast}}{3} \begin{bmatrix} 0 & 0 & 0 & 0 \\ 1 & -1 & -1 & 1 \\ 1 & 1 & -1 & -1 \end{bmatrix}$$

where each column is the centroid for one quadrant, starting from the $+Y/+Z$ quadrant and moving counterclockwise. l_{mast} is the length of the mast from the sail center to the tip. We see that for every quadrant,

$$|\vec{r}_{cm}| = \sqrt{2}\frac{l_{mast}}{3}$$

The geometric relationship between the RSB angle δ and the resulting sail angle θ is:

$$\begin{aligned} \sin\frac{\theta}{2} &= -\frac{\frac{1}{2}l_{bar}\sin\frac{\delta}{2}}{\frac{1}{2}l_{sail}} \\ \theta &\approx -2\frac{l_{bar}}{l_{sail}}\sin\frac{\delta}{2} \end{aligned}$$

as shown in Figure 3 on the following page. l_{bar} is the total length of the RSB and l_{sail} is the hypotenuse of the quadrant. The rotated stabilizer bar and sail each make an isosceles triangle which share an edge. The two approximations used are the small angle approximation for θ and $l_{bar}/2 \ll l_{mast}$. For this definition of the sail angle, a positive RSB rotation results in a negative sail angle.

The sail normals are defined in terms of θ as:

$$\hat{n}_{sail} = \begin{bmatrix} \cos\theta & \cos\theta & \cos\theta & \cos\theta \\ \frac{1}{\sqrt{2}}\sin\theta & \frac{1}{\sqrt{2}}\sin\theta & -\frac{1}{\sqrt{2}}\sin\theta & -\frac{1}{\sqrt{2}}\sin\theta \\ -\frac{1}{\sqrt{2}}\sin\theta & \frac{1}{\sqrt{2}}\sin\theta & \frac{1}{\sqrt{2}}\sin\theta & -\frac{1}{\sqrt{2}}\sin\theta \end{bmatrix}$$

The sun angle experienced by each sail quadrant is found from the dot product of its normal with the sun vector.

$$\begin{aligned} \gamma_{sun} &= \cos^{-1}(\hat{u}_{sun} \cdot \hat{n}_{sail}) \\ &= \cos^{-1}(\cos\alpha\cos\beta\cos\theta + \frac{1}{\sqrt{2}}\sin\theta \begin{pmatrix} \sin\alpha\cos\beta - \sin\beta \\ \sin\alpha\cos\beta + \sin\beta \\ -\sin\alpha\cos\beta + \sin\beta \\ -\sin\alpha\cos\beta - \sin\beta \end{pmatrix}) \end{aligned}$$

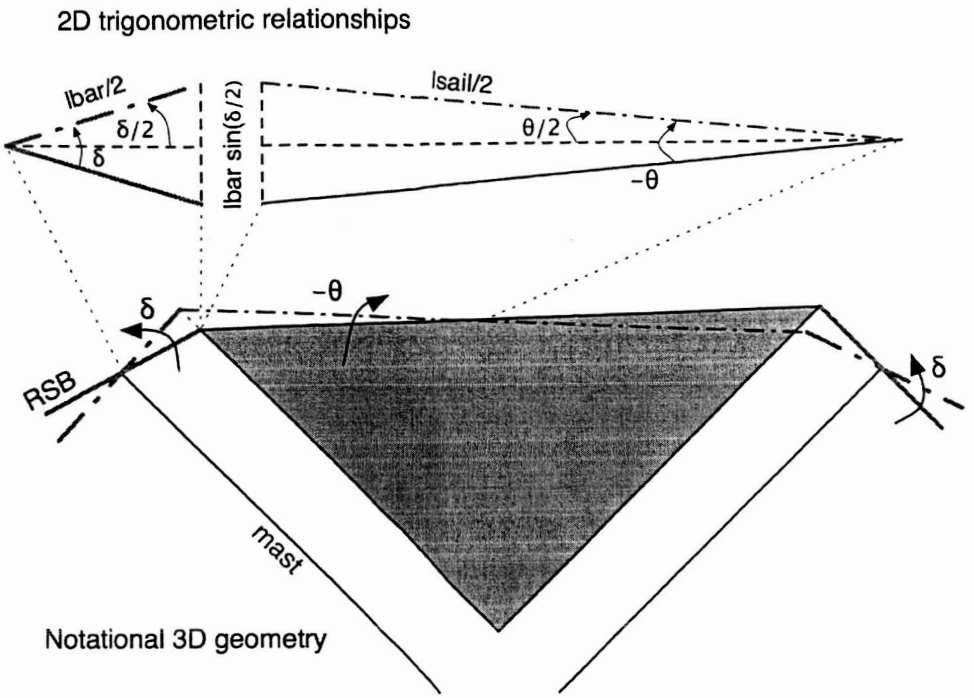

Figure 3. Relationship between RSB angle and sail angle

Thus, the result of twisting the sail quadrants in the presence of nonzero α and β sun angles is a different sun angle for each quadrant. Figure 4 indicates the sun angle each quadrant experiences for a small set of α and β angles and a full range of RSB angles.

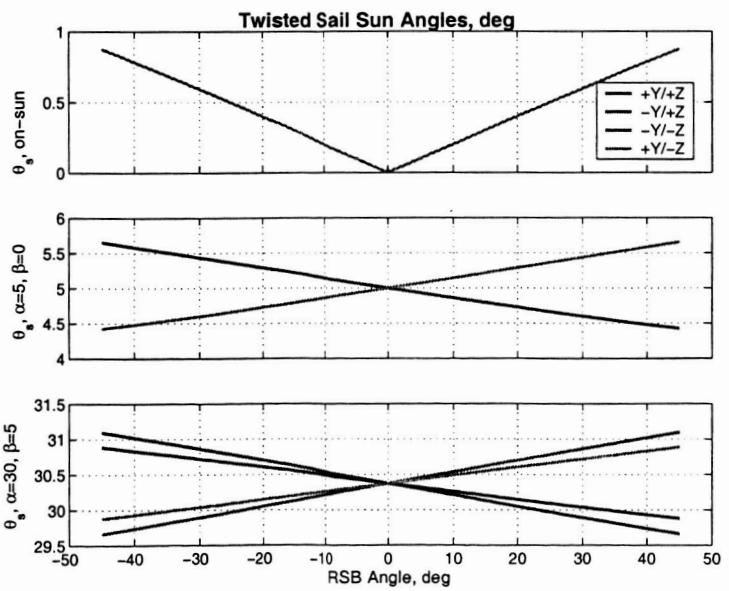

Figure 4. Example sun angles

The roll torque generated by rotating the sails, given a total solar pressure force F_{sun} aligned with the

X axis, can be simply approximated as

$$T = -F_{sun}\sqrt{2}\frac{l_{mast}}{3}\sin\theta = F_{sun}\sqrt{2}\frac{l_{bar}}{3}\sin\frac{\delta}{2}$$

since $l_{mast}/3$ is the moment arm to the centroid of the sail quadrant. However, for a nonaligned sun vector, the torque must be computed from

$$\vec{T} = \sum_i \vec{r}_{cm_i} \times \vec{F}_{s_i}$$

The solar force on each sail quadrant (excluding thermal effects) is

$$\vec{F}_{s_i} = p_s A \cos\gamma_{sun}(2(\sigma_s \cos\gamma_{sun} + \sigma_d/3)\hat{n} + (\sigma_a + \sigma_d)\hat{u}_s)$$

where

$$\sigma_a + \sigma_s + \sigma_d + \sigma_t = 1$$

Since the force depends on the effective area of each sail, the slightly different angles for each quadrant with respect to the sun vector results in a different force magnitude on each sail. Therefore while one might expect a pure roll torque from RSB actuation despite the angle of the sun vector, in reality the introduced mismatch between the sail forces results in torques along the pitch and yaw axes as well.

Writing out the cross products and summing over the quadrants gives

$$\vec{T} = |\vec{r}_{cm}| \begin{bmatrix} -4\sin\theta(\vec{F}_{s_1} + \vec{F}_{s_2} + \vec{F}_{s_3} + \vec{F}_{s_4}) \\ \frac{1}{\sqrt{2}}\cos\theta(\vec{F}_{s_1} + \vec{F}_{s_2} - \vec{F}_{s_3} - \vec{F}_{s_4}) \\ \frac{1}{\sqrt{2}}\cos\theta(-\vec{F}_{s_1} + \vec{F}_{s_2} + \vec{F}_{s_3} - \vec{F}_{s_4}) \end{bmatrix}$$

which, for a purely specularly reflective surface ($\sigma_a = \sigma_d = 0$), reduces to a dependence on the combinations of $\cos^2\gamma_i$.

Substituting the sun angle definitions in Equation 1 into the torque equation results in a lengthy equation we will not display, but we can easily consider the limiting cases. When $\beta = 0$, we have $F_1 = F_2$ and $F_3 = F_4$. In this case, a change in α leads to a nonzero T_y, but $T_z = 0$. Similarly, when $\alpha = 0$, $F_1 = F_4$, $F_2 = F_3$, β leads to a nonzero T_z, but $T_y = 0$. When both α and β are nonzero, then T_y and T_z are both nonzero as well.

An example is taken from 40 m square sail in a 6 pm DDSS orbit, given in Table 1. The angle between the sun vector and the orbit normal varies with both the orbit period and time of year. The sail is nominally aligned with the LVLH frame to prevent gravity gradient torques, with a -90 degree yaw (z) rotation to bring the sail from edge-on the sun to approximately full-on. Figure 5 on the next page indicates the sun angles (azimuth, elevation, and total angle) and the RSB torque so that the connection between them is clear. The torque is calculated for an RSB angle of 10 degrees (sail angle of 0.19 degrees) and sail tack angles of 0 and 30 degrees, that is, LVLH yaw angles of -90 and -60 degrees. Note that even for a tack angle of zero degrees, the sail experiences about an 11 degree sun angle due to the LVLH alignment.

Table 1. DDSS Epoch and Orbital Elements

Year	Month	Day	H	M	S
2010	3	15	16	0	0
a (km)	**i (rad)**	**Ω (rad)**	**ω (rad)**	**e**	**M**
7971	1.7891	1.5708	3.022	0	0

From these, one can clearly see that rotating the stabilizer bars creates pitch and yaw torques in addition to roll torques when the sail is not perfectly aligned with the sun. These torques oscillate at orbit rate due to the oscillation in the LVLH sun angles around the orbit, but the mean value is approximately zero whereas the roll torque is constant. Increasing the sail's tack angle in this orbit to 30 degrees creates a large offset in the sun's azimuth angle (green lines). This is turn creates an offset in the pitch torque, while only slightly changing the amplitude of the yaw torque. The small change in yaw torque with tack angle is because, as we mentioned previously, T_y is more strongly linked to α than T_z, and in this case α changes a lot with the

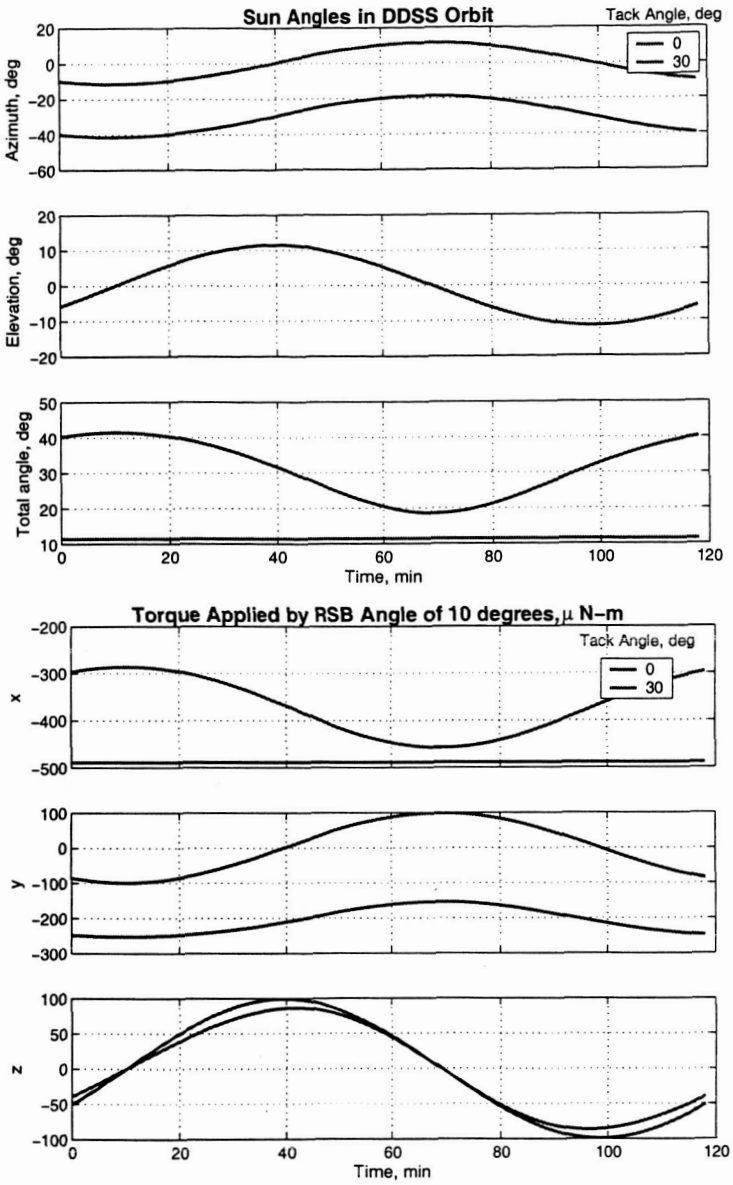

Figure 5. An Example of RSB Torque

tack angle while β remains about the same. In general, the geometry of the sun vector, and not just the magnitude of the sun angle or the sail angles, drives the resulting three-axis torque distribution. The roll torque does remain dominant, indicating that the RSBs are still an effective actuator if sufficient pitch and yaw control is also available. The off-axis torques could be directly accommodated by feedforwarding the torque estimates to the pitch/yaw controller, improving the overall peformance.

This calculation has been compared to the full disturbance model, which includes a complete CAD description of the components and multiple disturbance types. The torque from the disturbance model for a 30°tacked sail, on the right in Figure 6 on the following page, is comparable to the output for a tacked sail from this derivation (green line) which uses only solar radiation pressure (SRP), validating this flat-plate analysis approach for this model.

Lastly, we consider a closed-loop simulation with a PD controller and the full disturbance model in Figure 8 on page 8. The commanded maneuver is a 30 degree slew in yaw from a a sun-facing attitude. The roll axis inertia is roughly twice the other axis, so we see the effects of Euler coupling. We can see that

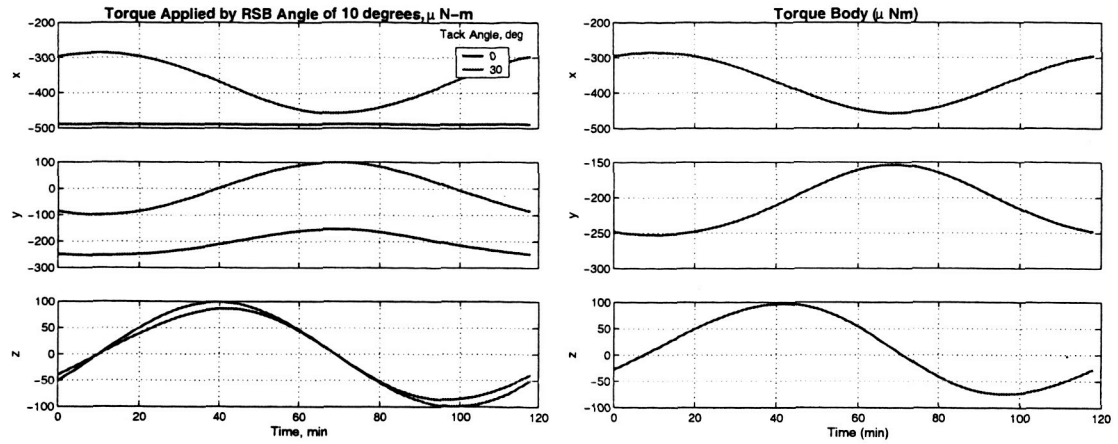

Figure 6. Comparison of Calculated SRP Torque (left) and Disturbance Model Output for 30 degree Tacked Sail (right)

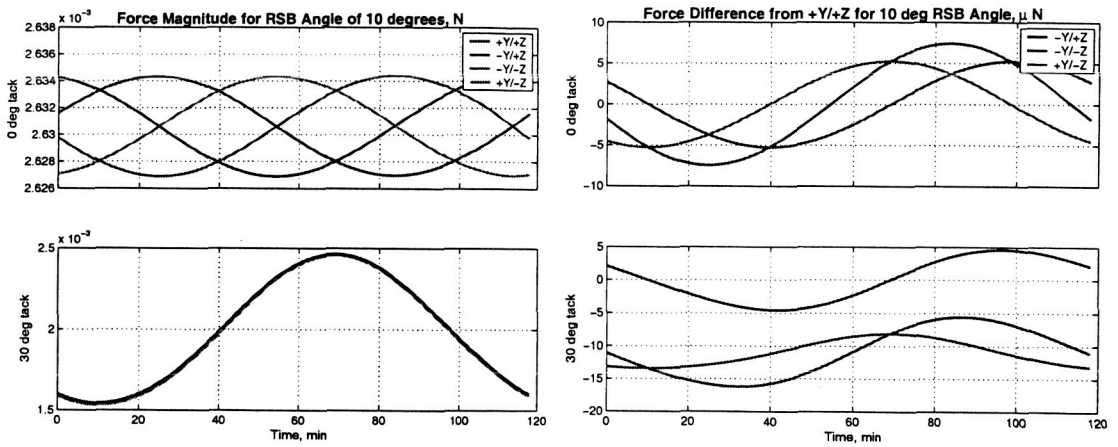

Figure 7. Calculated SRP Forces

both the roll and pitch axes become involved but that the attitude stabilizes, since we have enough control authority in the TCMs.

III. Trim Control Mass Analysis

The equations of motion for a two phase stepper motor in ab coordinates (physical, orthogonal winding axes) are[1]

$$\begin{aligned} \frac{di_a}{dt} &= \frac{1}{L}\left(v_a - Ri_a + K_m\omega sin(N_r\theta)\right) \\ \frac{di_b}{dt} &= \frac{1}{L}\left(v_b - Ri_b - K_m\omega cos(N_r\theta)\right) \\ \frac{d\omega}{dt} &= \frac{1}{J}\left(K_m i_b cos(N_r\theta) - K_m i_a sin(N_r\theta) - B\omega\right) \\ \frac{d\theta}{dt} &= \omega \end{aligned} \tag{1}$$

where i_a and i_b are the phase currents, v_a and v_b are the phase voltages which will be used for control, N_r is the number of rotor teeth, L is the inductance of the windings, R is the winding resistance and K_m is the motor torque constant in units of Nm/A, ω is the rotor angular rate and θ is the rotor angle. J is the rotor inertia. Each phase winding is assumed to have the same resistance and inductance. The response is shown in Figure 9 on the following page.

The phase voltages switch and the rotor moves to the new position. The stepper motor in effect has its own feedback loop to maintain the position so no external feedback position control is required. The stepper

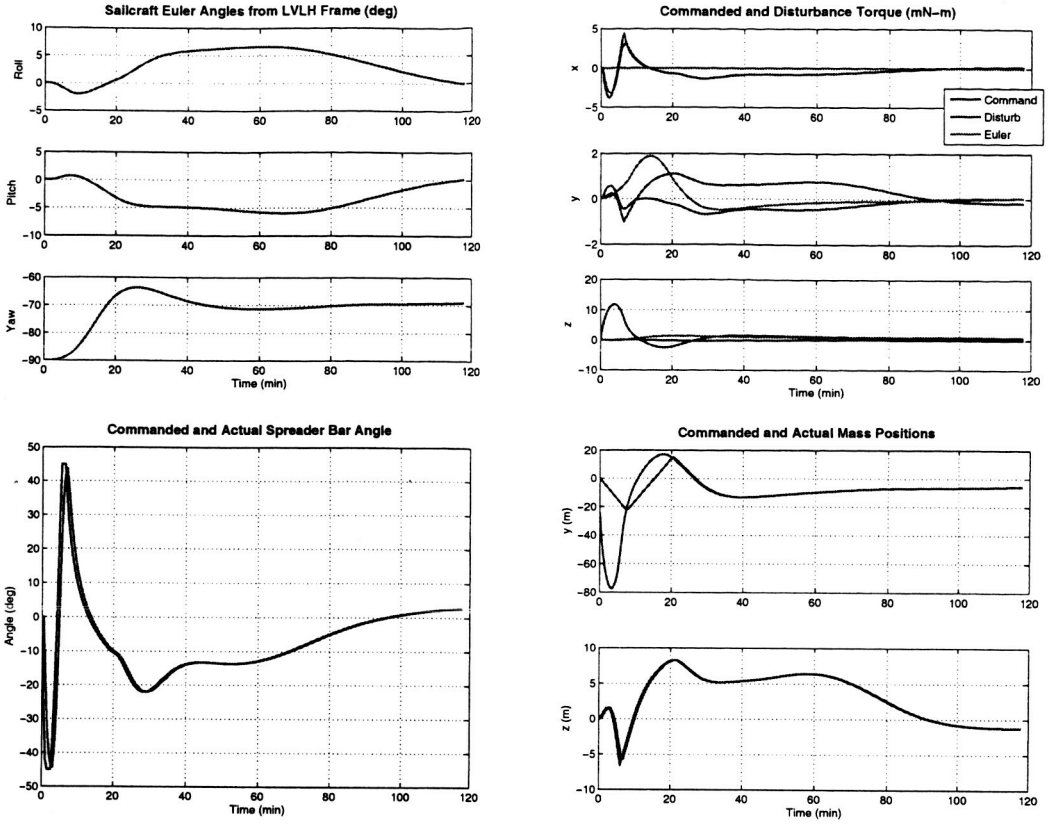

Figure 8. DDSS Closed-Loop Simulation with TCMs and RSBs

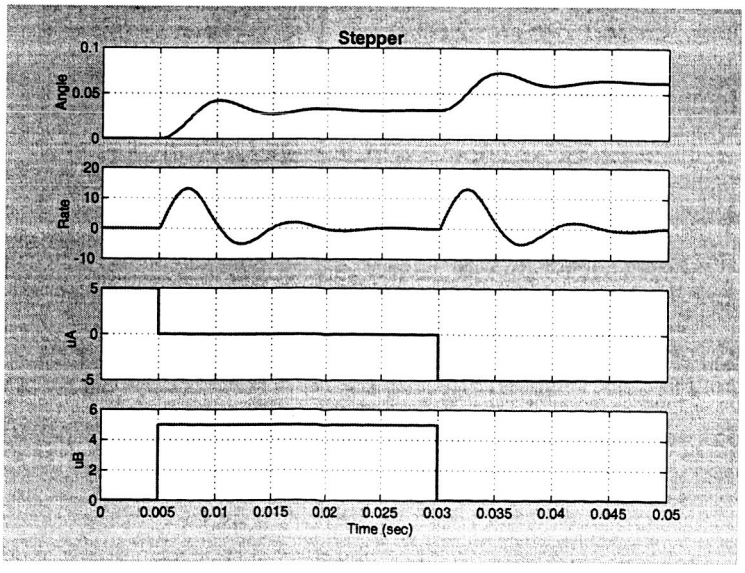

Figure 9. stepper motor response

motor dynamics are very high frequency so it is not necessary to model the dynamics when analyzing the solar sail control system.

For the purpose of simulations we can assume the trim control masses can attain any speed instantaneously, i.e. they do not accelerate. Angular momentum of the system must be conserved, so when the masses are moving the vehicle rates must be adjusted accordingly. An example of a 70 degree pitch maneuver for a 160 m, 450 kg sail in SPI transfer orbit with 5 kg moving masses[7] is shown in Figure 10. The moving mass velocity is limited to 5 cm/s. The disturbance model consists of solar radiation pressure on purely specular flat plate quadrants. The controller is a PID with a bandwidth of 0.001 rad/s.

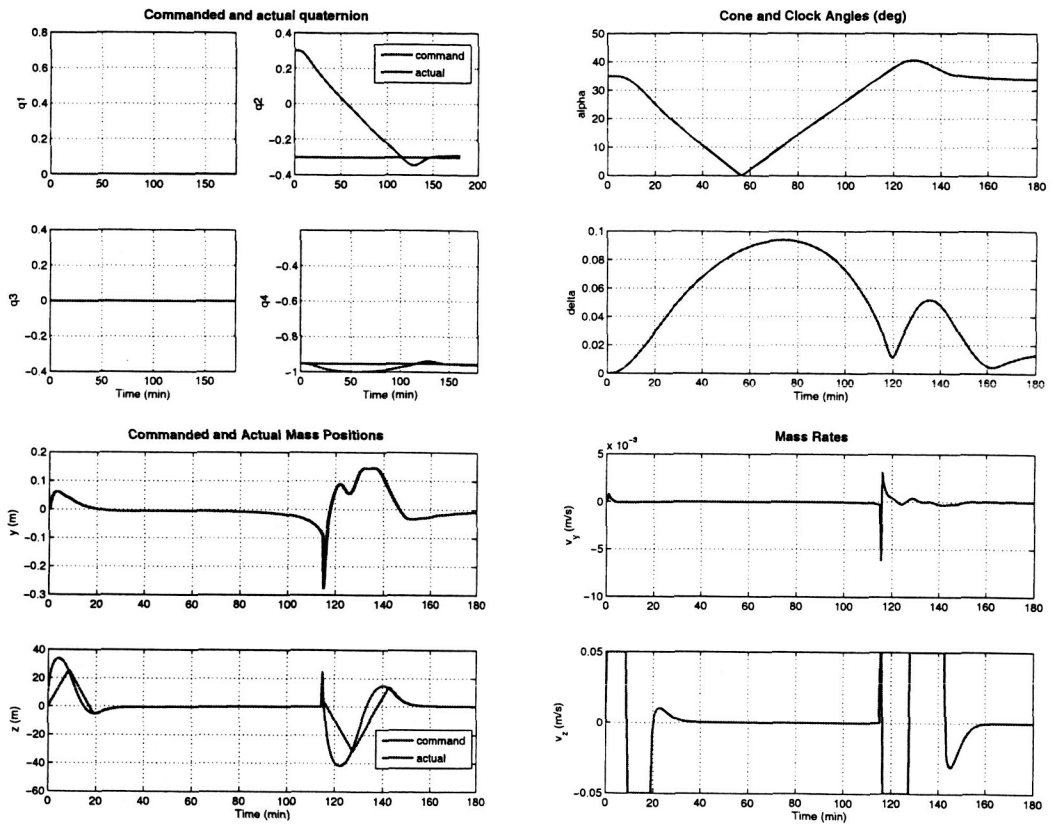

Figure 10. Moving mass actuation demo for a rigid model in SPI orbit

IV. Sail FEM Model

The model under study is the 20 m workhorse sail recently deployed at NASA Glenn Research Center Plum Brook Station (Sandusky, OH) by ATK Space Systems (Goleta, CA).[3] A 1028 node finite-element model is available for this sail. The first 30 modes range from about 0.5 to 1 Hz. The model and modes can be effectively visualized in MATLAB as seen in Figure 11 on the following page.

One control method under consideration is a suite of pulsed plasma thrusters mounted at the tip of the masts.[6] On the $+Y$ axis for this model, the corresponding node at which the force will be applied is 40001. A $+X$ force applied here will produce a negative rotation about the Z axis.

We require a state-space form of the dynamics, i.e.

$$\begin{aligned} \dot{x} &= Ax + Bu \\ y &= Cx + Du \end{aligned}$$

Our vehicle consists of a rigid core and a flexible appendage. We begin by defining a set of nodes on the appendage. If the vector from system center of mass (C_{sys}) to the origin is c, and the nodal displacements

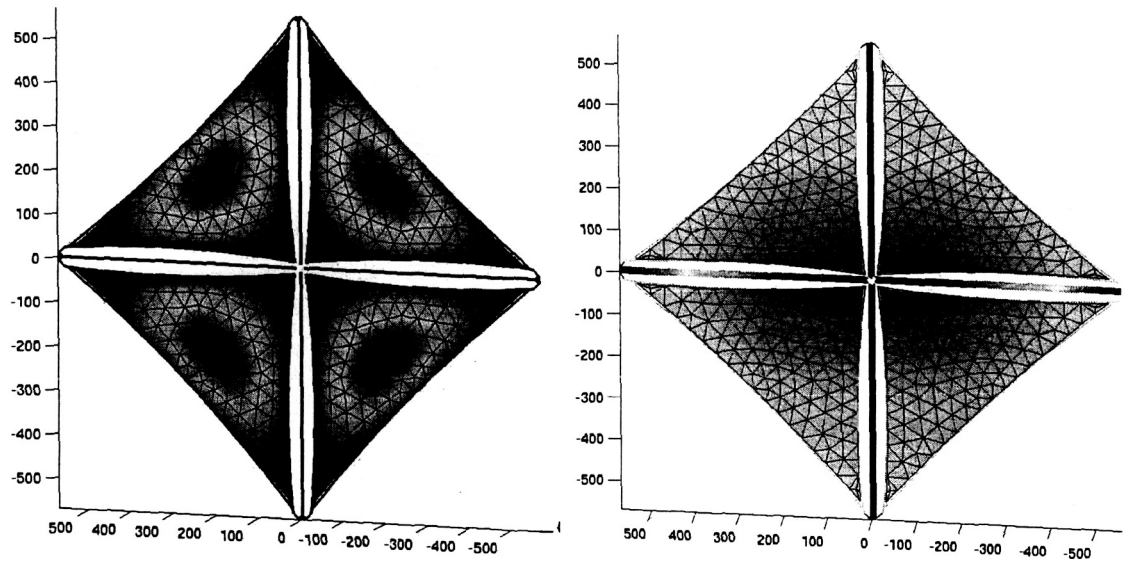

Figure 11. Solar sail mode visualization in MATLAB; on the left, mode 1, on the right, mode 22.

are ρ_k, then the vectors from C_{sys} to the nodes are $d_k = c + r_k + \rho_k$. This is depicted in Figure 12.

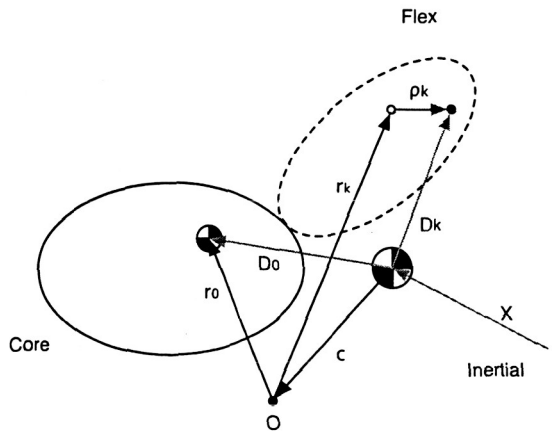

Figure 12. Node vector definitions

We also define the modal displacements η, where the transformation matrix Φ gives the nodal displacement per unit modal displacement for each mode. Φ is constructed as a $3n$ by m matrix, where n is the number of nodes and m is the number of modes. This can be written compactly in matrix notation as

$$\rho = \Phi\eta \tag{2}$$

Our goal is to develop state-space equations using the modal coordinates. We begin with the total angular momentum of a rigid core with a flexible body about the spacecraft center-of-mass. Note that the sum includes the displacement of the core from the system center of mass.

$$H = A(I\omega) + \sum_{k=0}^{n} m_k D_k^{\times} \dot{D}_k \tag{3}$$

where A is the rotation from the body frame to the inertial frame and $D_k = Ad_k$ is in the inertial frame.

Taking the inertial derivative and transforming to the body frame we have

$$T = I\dot{\omega} + \omega^{\times} I\omega + \sum_{k=0}^{n} m_k d_k^{\times} \ddot{d}_k \tag{4}$$

where I is the inertia matrix of the core and T is the external torque on the spacecraft. The definition and derivatives of d are

$$\begin{aligned} d &= r + c + \rho \\ \dot{d} &= \omega^{\times} d + \dot{\rho} + \dot{c} \\ \ddot{d} &= \omega^{\times}\omega^{\times} d + \dot{\omega}^{\times} d + 2\omega^{\times}(\dot{\rho} + \dot{c}) + \ddot{\rho} + \ddot{c} \end{aligned}$$

where c, assuming r_0 is zero, is

$$c = -\sum_{k=1}^{n} \frac{m_k(r_k + \rho_k)}{m_T} \tag{5}$$

Next we write the inertial equations of motion for each nodal mass, including the motion of the spacecraft center-of-mass, $\ddot{X}$, produced by the total external force. We drop the nonlinear terms in ω, $\dot{\rho}$ and $\dot{c}$.

$$f_k = m_k(\ddot{d}_k + \ddot{X}) \tag{6}$$

$$f_k \approx m_k(-d_k^{\times}\dot{\omega} + \ddot{\rho}_k + \ddot{c} + \frac{\sum F}{\sum m}) \tag{7}$$

where f_k is the sum of the internal forces exerted by adjacent nodes and any external forces on the nodes. The internal mass forces can also be represented as a spring force, giving

$$f_k = -\sum_j k_{kj}(\rho_j - \rho_k) + F_k \tag{8}$$

where k is a physical property of the structure and F_k are the external forces. Substituting this force definition and the definition of c we have

$$m_k(\ddot{\rho}_k + \ddot{c}) + K\rho = -m_k(-d_k^{\times}\dot{\omega} + \frac{\sum F}{\sum m}) + F_k \tag{9}$$

$$m_k(\ddot{\rho}_k - \sum \frac{m_j \ddot{\rho}_j}{m_T}) + K\rho = m_k d^{\times}\dot{\omega} + \frac{m_T - m_k}{m_T} F_k - m_k \sum_{j \neq k} \frac{F_j}{m_T} \tag{10}$$

$$m_k(\frac{m_T - m_k}{m_T}\ddot{\rho}_k - \sum_{j \neq k} \frac{m_j \ddot{\rho}_j}{m_T}) + K\rho = m_k d_k^{\times}\dot{\omega} + \frac{m_T - m_k}{m_T} F_k - m_k \sum_{j \neq k} \frac{F_j}{m_T} \tag{11}$$

$$m_k(\nu_k \ddot{\rho}_k - \sum \mu_j \ddot{\rho}_j) + K\rho = m_k d_k^{\times}\dot{\omega} + \nu_k F_k - \mu_k \sum F_j \tag{12}$$

where K is symmetric and full. For three-dimensional displacements, ρ is $3n$ x 1 and K is $3n$ x $3n$. Now we assign $\tilde{M}$ to be the coefficients of $\ddot{\rho}$ and N to be the coefficients of F, and we have in matrix form

$$\tilde{M}\ddot{\rho} + K\rho = Md^{\times}\dot{\omega} + NF \tag{13}$$

Φ for the cantilevered flex modes is normalized so that the modal masses are equal to one and

$$\Phi^{\mathrm{T}} M \Phi = E$$

$$\Phi^{\mathrm{T}} K \Phi = \Omega^2$$

Therefore, switching now to modal coordinates and making the above substitutions in Equation 13 we have

$$\begin{aligned} \tilde{M}\Phi\ddot{\eta} + K\Phi\eta &= Md^{\times}\dot{\omega} + NF \\ \Phi^{\mathrm{T}}\tilde{M}\Phi\ddot{\eta} + \Phi^{\mathrm{T}}K\Phi\eta &= \Phi^{\mathrm{T}}(Md^{\times}\dot{\omega} + NF) \\ \Phi^{\mathrm{T}}\tilde{M}\Phi\ddot{\eta} + \Omega^2\eta &= \Phi^{\mathrm{T}}(Md^{\times}\dot{\omega} + NF) \end{aligned} \tag{14}$$

This is comparable to the general form of a modal dynamics equation for a flexible system (including damping),[2]

$$\ddot{\eta} + 2Z\Omega\dot{\eta} + \Omega^2\eta = Bu \tag{15}$$

where Z is the modal damping matrix and u are the nodal inputs, except that having $\tilde{M}$ will result in the free frequencies being higher than the cantilevered frequencies.

Next we move to development of the torque equation (4). First we write an intermediate step of the equation by substituting in the equation for $\ddot{d}$, neglecting only the nonlinear terms in $\dot{\rho}$ and $\dot{c}$:

$$T = I\dot{\omega} + \omega^\times I\omega - \sum_{k=0}^{n} m_k d_k^\times (\omega^\times\omega^\times d_k - d_k^\times\dot{\omega} + \ddot{\rho}_k + \ddot{c}) \tag{16}$$

The total inertia I_T is defined as $I_T = I_{core} - \sum m_k d_k^\times d_k^\times$. We gather terms which contribute to I_T, note that the sum of the coefficients of $\ddot{c}$ is zero and ρ_0 is also zero, and convert to modal coordinates:

$$T = [I - \sum_{k=0}^{n} m_k d_k^\times d_k^\times]\dot{\omega} + \omega^\times[I - \sum_{k=0}^{n} m_k d_k^\times d_k^\times]\omega - \sum_{k=1}^{n} m_k d_k^\times \Phi\ddot{\eta} \tag{17}$$

The torque T is the sum of all external torques, including any forces applied at the nodes.

$$T = T_c + \sum d_k^\times F_k \tag{18}$$

We can now write both the core and mass equations in matrix form with the terms containing $\dot{\omega}$ and $\ddot{\eta}$ on the left.

$$\begin{bmatrix} I_T & \sum_k m_k d_k^\times \phi_{k,1} & \cdots & \sum_k m_k d_k^\times \phi_{k,m} \\ [\sum_k m_k d_k^\times \phi_{k,1}]^{\mathrm{T}} & & & \\ \vdots & & \Phi^{\mathrm{T}}\tilde{M}\Phi & \\ [\sum_k m_k d_k^\times \phi_{k,m}]^{\mathrm{T}} & & & \end{bmatrix} \begin{bmatrix} \dot{\omega} \\ \ddot{\eta}_1 \\ \vdots \\ \ddot{\eta}_m \end{bmatrix} = \begin{bmatrix} -\omega^\times I_T\omega \\ -\Omega^2\eta \end{bmatrix} + \begin{bmatrix} T \\ \Phi^{\mathrm{T}}NF \end{bmatrix}$$

The left-hand matrix summation terms can be considered a generalized modal inertia matrix, I_{modal}. The terms indicate the contribution for each mode, which is a sum over the contributions from each node. Grouping these terms into a matrix and explicitly writing out the core and node inputs we have

$$\begin{bmatrix} I_T & I_m \\ I_m^T & \Phi^{\mathrm{T}}\tilde{M}\Phi \end{bmatrix} \begin{bmatrix} \dot{\omega} \\ \dot{\eta} \end{bmatrix} = \begin{bmatrix} (I_T\omega)^\times & 0 & 0 \\ 0 & -\Omega^2 & -2Z\Omega \end{bmatrix} \begin{bmatrix} \omega \\ \eta \\ \dot{\eta} \end{bmatrix} + \begin{bmatrix} E_3 & d_0^\times & d_k^\times \\ 0 & \frac{\sum m_k \Phi^{\mathrm{T}}}{M} & \Phi^{\mathrm{T}} \end{bmatrix} \begin{bmatrix} T_c \\ F_c \\ NF_k \end{bmatrix} \tag{19}$$

To obtain a state-space form from this equation, we will have to divide by the inertia matrix on the left and add kinematics. In addition, we have left in the $(I\omega)^\times$ nonlinear term for now, which will need to be linearized. There are two common cases, first the presence of a large bias momentum (such as a momentum wheel) and second for a steady body rate. In the case of bias momentum and small body rates, the bias drives the nonlinear term and the linearized version is simply

$$\omega^\times I\omega \approx -h_B^\times\omega$$

In the case of a steady rate, we linearize around the rate and drop terms of second order.

$$\begin{aligned} \omega^\times I\omega &= (\omega+\omega_0)^\times I(\omega+\omega_0) \\ &\approx (-(I\omega_0)^\times + \omega_0^\times I)\omega + \omega_0^\times I\omega_0 \end{aligned}$$

To complete our state-space representation we need to add states for the attitude. We consider three easily linearized cases, small Euler angles, small quaternion deviations, and perturbations from a rotating frame. Small 3-2-1 Euler angles can be integrated to first order directly from the body rates, giving

$$\dot{\theta} = \begin{bmatrix} 0 & E \end{bmatrix} \begin{bmatrix} \theta \\ \omega \end{bmatrix}$$

If the spacecraft is undergoing a steady rotation and we designate the nominal rate vector as ω_0, then the angular velocity is simplified with the small angle approximation as follows,

$$\omega \approx \dot{\theta} + (E - \theta^{\times})\omega_0$$

Rearranging to solve for $\dot{\theta}$ we have

$$\dot{\theta} = \begin{bmatrix} -\omega_0^{\times} & E \end{bmatrix} \begin{bmatrix} \theta \\ \omega \end{bmatrix} - \omega_0$$

For small angle quaternions, the first component (q_s) is constant and the derivative reduces to one-half the body rates for the latter three terms (q_r),

$$\begin{bmatrix} \dot{q}_s \\ \dot{q}_r \end{bmatrix} = \begin{bmatrix} 0 & 0 & 0 \\ 0 & 0 & \frac{1}{2}E \end{bmatrix} \begin{bmatrix} q_s \\ q_r \\ \omega \end{bmatrix}$$

V. Simple Non-Collocated Systems

Using a PPT at the tip of the solar sail with sensing at the core is a classic noncollocated problem. However, compensating such a system near the flex modes is not trivial and bears review. We first analyze one dimensional and planar systems before moving to the full sail model.

A. One-dimensional system

We begin our control analysis by compensating a simple 1 dimensional two-mass, one-spring system with a non-collocated sensor and actuator.

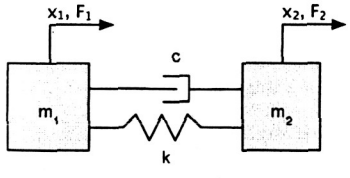

$$m_1\ddot{x}_1 + c(\dot{x}_1 - \dot{x}_2) + k(x_1 - x_2) = F_1 \quad (20)$$
$$m_2\ddot{x}_2 + c(\dot{x}_2 - \dot{x}_1) + k(x_2 - x_1) = F_2 \quad (21)$$

In the frequency domain, neglecting damping for the moment, the system becomes

$$\begin{bmatrix} x_1 \\ x_2 \end{bmatrix} = \frac{\begin{bmatrix} s^2 + w_2^2 & w_1^2 \\ w_2^2 & s^2 + w_1^2 \end{bmatrix} \begin{bmatrix} F_1/m_1 \\ F_2/m_2 \end{bmatrix}}{s^2(s^2 + (w_1^2 + w_2^2))} \quad (22)$$

where $\omega_1^2 = k/m_1$ and $\omega_2^2 = k/m_2$. From this we see that for the collocated case F_2 to x_2, at low and high frequencies relative to the flex resonance the system acts like a rigid body, $1/s^2$. The lead from the zero(s) is cancelled by the lag from the pole(s) so that the phase after the flex frequencies remains 180. For F_2 to x_1, however, at high frequencies the denominator approximates $1/s^4$, resulting in permanent phase lag. This is easily seen in the open loop response for both cases in Figure 13 on the following page.

The system properties are selected to give a natural frequency near the lowest sail mode. m_1 is 10 kg, m_2 is 1 kg, k is 0.3, c is 0.03, ω_n is 0.574 and $\Phi = [0.0953 \quad -0.953]$.

We first apply a forward gain for the desired transient response, $k = 0.01$. The result is unstable. We then add phase lead at the crossover frequency for the desired damping, with a maximum phase shift of 40 degrees at $w_{max} = 1^{-2}$. This pushes the crossover frequency up, so we lower the gain to 0.001 and raise w_{max} to 2e-2, which gives a stable system. There is now a tradeoff between amount of phase lead and excitation of the flex mode. Figure 14 on the next page shows the open loop and step responses for phase leads of 40 and 65.

Next we add a notch filter to reduce the gain seen by the flex mode. This should allow us to use the higher phase lead (i.e. more damping) with less excitation of the mode. We set the notch frequency equal to the resonant frequency (0.574 Hz) with a gain reduction of 20 dB and a notch width of 0.1 Hz. See Figure 15 on page 15.

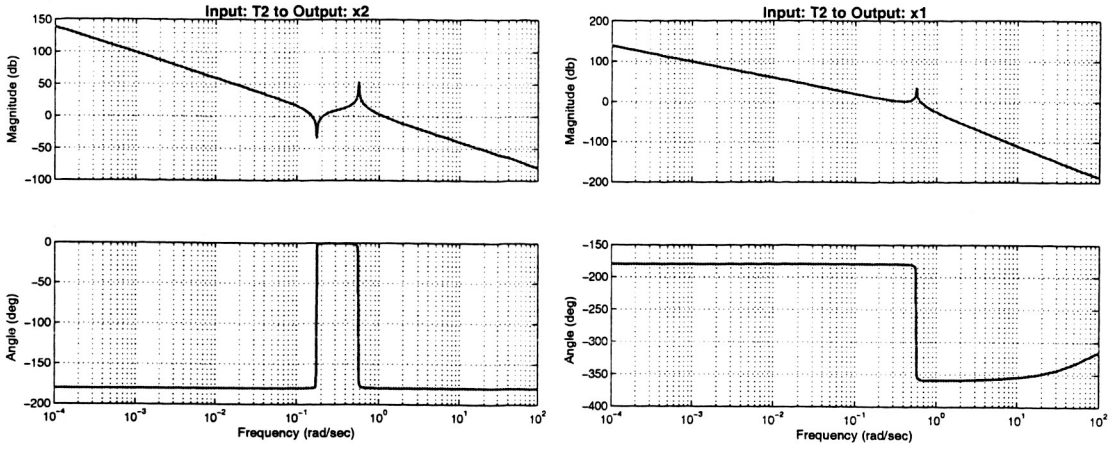

Figure 13. Open loop response for collocated and non-collocated actuation

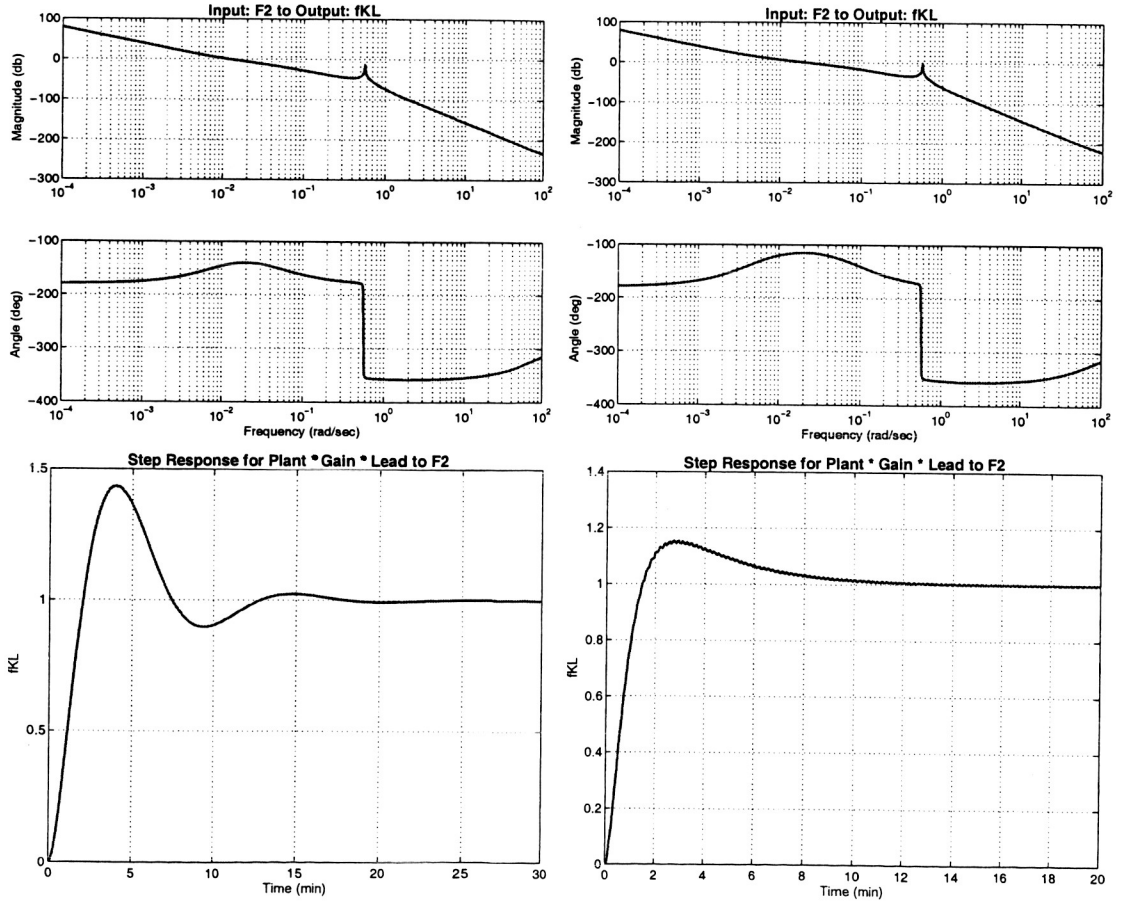

Figure 14. Trade-off between phase lead (damping) and mode excitation, for a phase lead of 40 degrees on the left and 65 degrees on the right

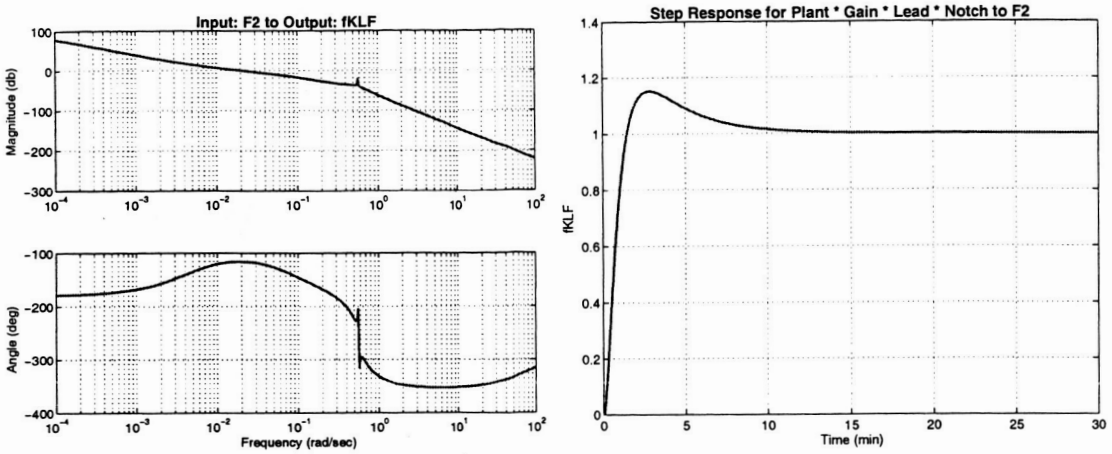

Figure 15. Compensator with a notch filter at the flex mode

Lastly, we need to add an integrator to drive the offset to zero. We will need this in the solar sail controller since the pointing during delta-V changes controls the thrust vector; we essentially want to limit the average pointing error over a maneuver within some tolerance. There is a trade between the time constant of the integrator and the forward gain; an infinitely high gain would result in a negligible offset, and correspondingly adding the integrator should allow for a higher gain. We will use a slow integrator of 3600 s, and add it in parallel with the lead compensator and filter.

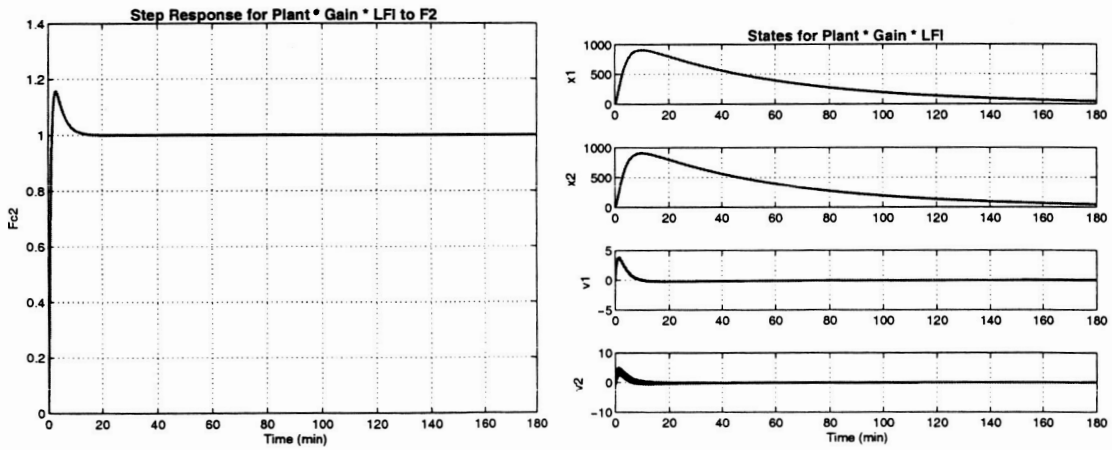

Figure 16. Compensator with integrator added in parallel

This same loop shaping procedure can be used with more complex systems such as the solar sail.

B. Planar system

Now that we have established the response and control of the simplest flex system, we check our theoretical development for n flex nodes with a rotational planar system consisting of a core and two masses, having two flex frequencies. The core mass is 100 kg, m_1 is 2 kg and r_1 is 2 m, and m_2 is 1 kg and m_2 is 4 m, and the flex displacements are transverse to the node locations, as shown in Figure 17 on the next page. For a spring stiffness of 0.5, the cantilevered natural frequencies are 0.38268 and 0.92388 rad/sec. If the flex body is correctly linked to the core, we expect that the response to a force at r_2 will be 4 times the response to a unit torque on the core. We see in Figure 18 on the following page that we do get the collocated and noncollocated responses we expect. Note the upward shift of the flex frequencies from the cantilevered frequencies to the free frequencies.

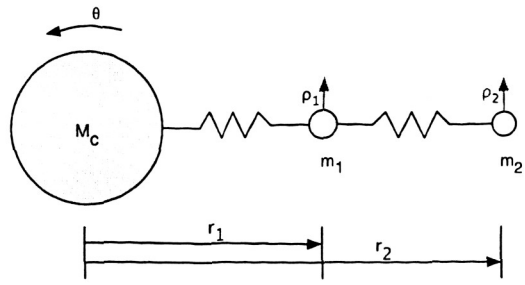

Figure 17. Simple rotational system

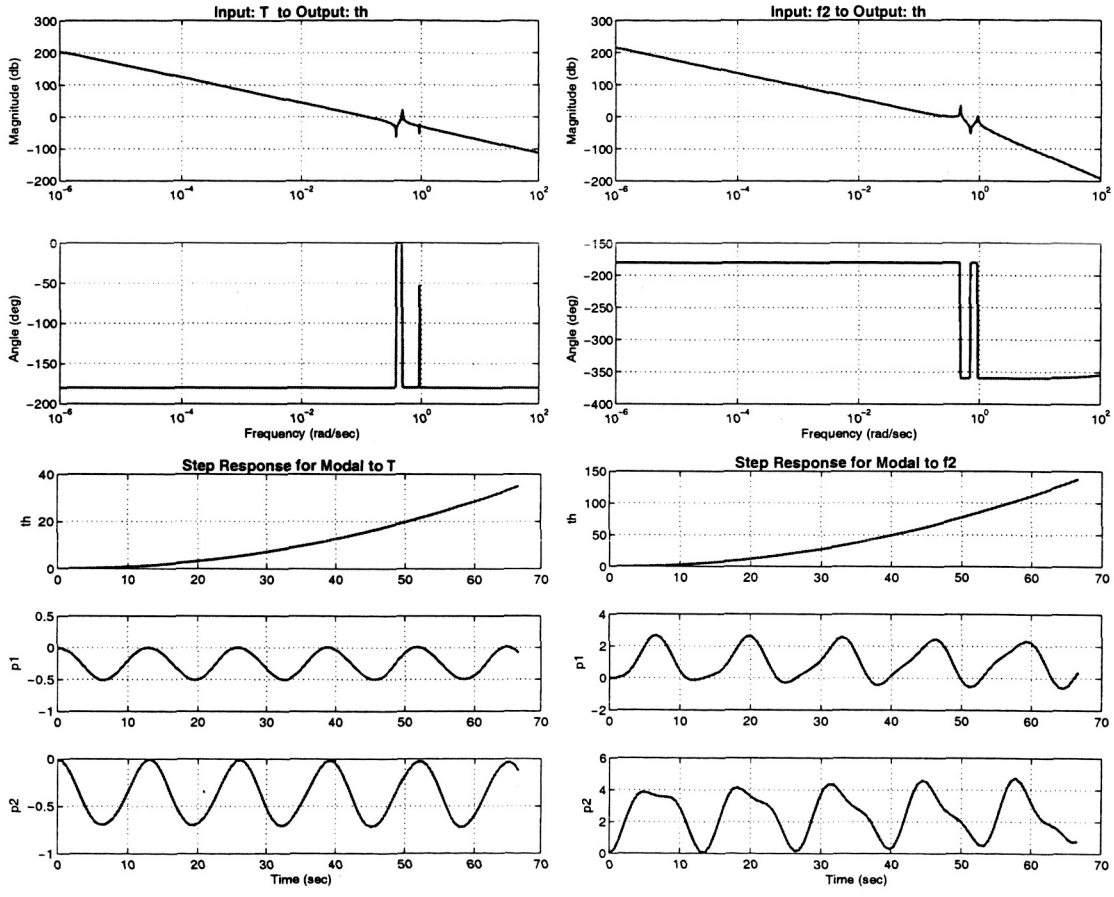

Figure 18. Response for a core with a 2 node flex body

VI. Solar Sail Analysis

In the case of the 20 m sail, the flex frequencies are relatively high and a PID controller would be sufficient for actuation at 0.002 rad/s bandwidth.[7] For larger sails, the modes will scale as some combination of the boom modes, a $1/L^2$ relationship, and the membrane modes, a $1/L$ relationship, so that the flex modes and bandwidth will be considerably closer. There is also the complication that there are many modes very close together, so that with overlapping poles and zeros we may not see the clear noncollocated response in the simple models.

First we check the open-loop sail plant with our desired force input at a boom tip. We choose a node on the $+Y$ boom and consider forces in the $+X$ and $+Z$ directions, which will produce respectively $-T_z$ and

$+T_x$. The inertia about the X axis is twice that of the other axes, and the boom tip is about 14.4 m from the core center. This is a complex system, and we do not see a simple noncollocated response in both cases when considering the first 8 modes. For F_x, we see a rigid body response (Figure 19), but for F_z, which interacts strongly with only one of the 30 given modes (η_8), we do see a phase drop.

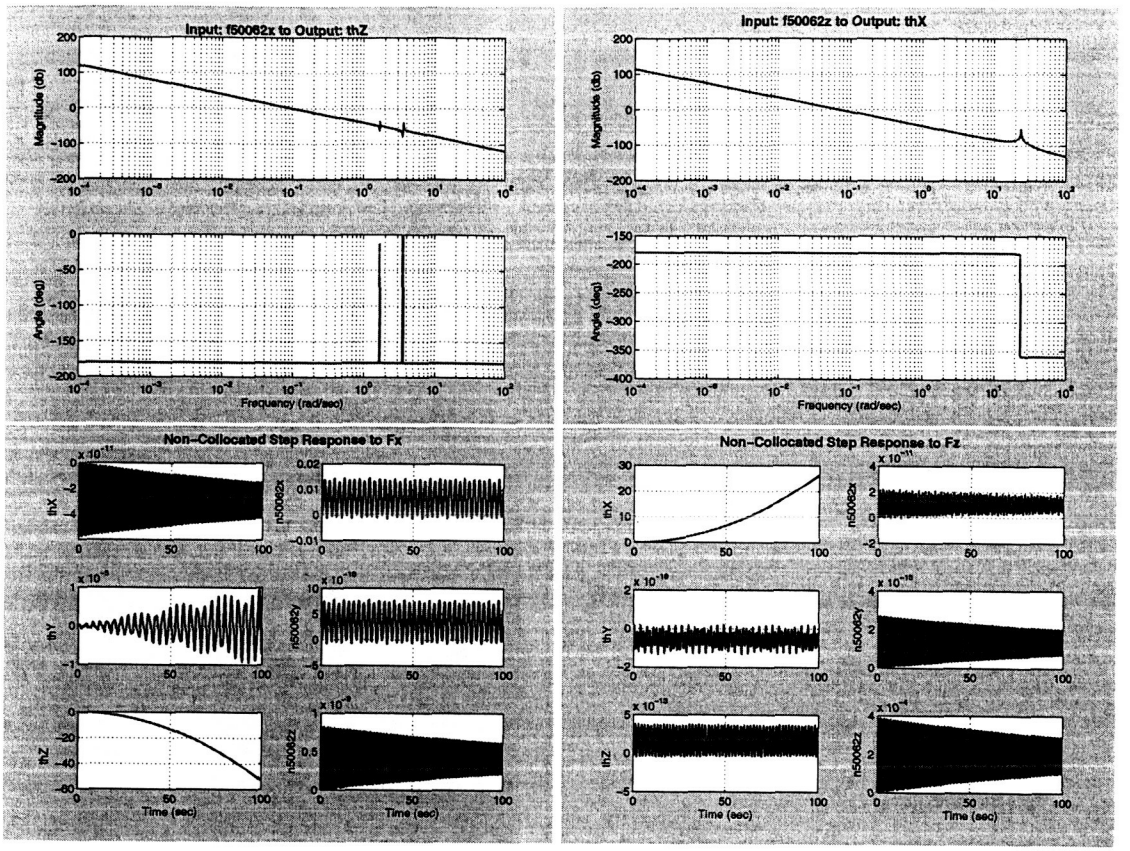

Figure 19. Frequency Response including Modes 1-8

We are interested in developing a controller which may have structural interactions as may occur for larger sails. We apply a PID controller at different control frequencies, again keeping modes 1-8 in the plant, and check the eigenvalues for stability. For w_n equal to 0.001 and 0.01 rad/sec, the PID controller is stable with the noncollocated actuation at the tips; at 0.1 however it is not, so this provides an opportunity to try the loop shaping procedure outlined in Section V on page 13.

We will compensate the roll axis since it has an interesting noncollocated response. We begin with a gain of 0.6, max phase frequency of 0.2, and a phase gain of 65 degrees. Then we add a notch filter at the apparent flex frequency, about 24 rad/sec, with a half-notch width of 5 rad/sec and a gain drop of -20 dB. See Figure 20 on the next page and Figure 21 on the following page.

VII. Conclusions

We have analyzed the proposed trim control mass (TCM) and roll stabilizer bar (RSB) actuators and concluded that it is not necessary to simulate the motor dynamics of the TCMs. The RSBs can produce the needed roll control torques but will require compensation for the off-axis torques induced by the sun vector geometry.

We have demonstrated that a relatively simple controller can be used to control a flexible system, including the solar sail with tip-mounted actuators. So far we have used idealized actuation and assumed damping in the system. In future work, we will incorporate realistic damping, actuator, and sensor models into models of . We would perform simulations with the linearized flex plant developed here, a nonlinear core model,

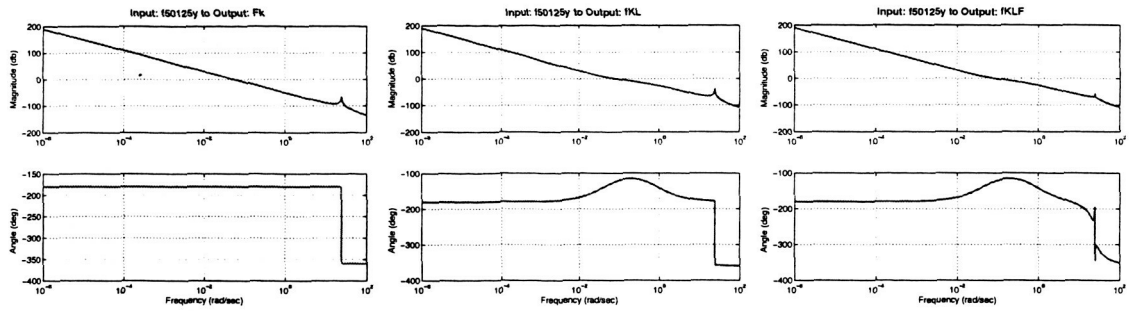

Figure 20. Frequency response of compensated sail (including modes 1-8), with a pure gain, gain with lead compensation, and compensator with notch filter.

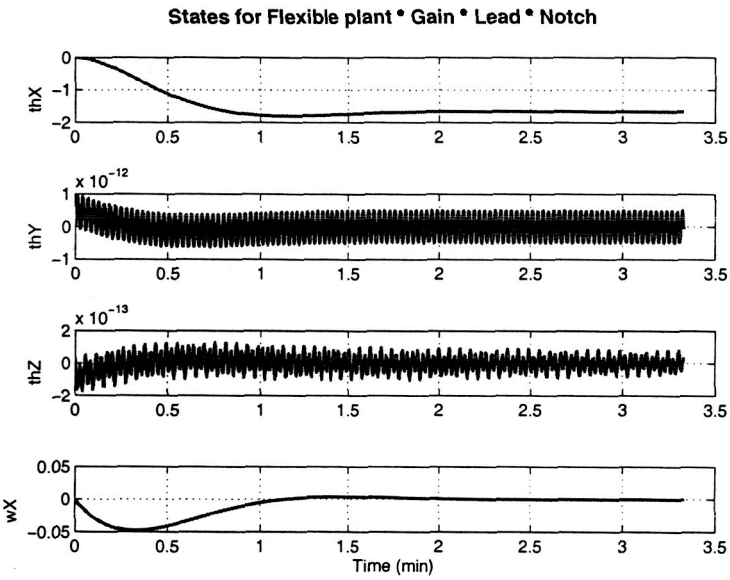

Figure 21. Step response of compensated sail (including modes 1-8)

nonlinear sensor and actuator models to demonstrate large angle slews and other maneuvers.

In analyzing the inputs at a single node we have shown that the structure flex interactions are complex and do not necessarily follow simple models. The sail has many closely-spaced frequencies and deciding which modes to include in higher-fidelity studies will require detailed analysis.

Acknowledgments

The work described in this paper was funded in whole or in part by the In-Space Propulsion Technology Program, which is managed by NASA's Science Mission Directorate in Washington, D.C., and implemented by the In-Space Propulsion Technology Office at Marshall Space Flight Center in Huntsville, Alabama. The program objective is to develop in-space propulsion technologies that can enable or benefit near and mid-term NASA space science missions by significantly reducing cost, mass or travel times. The authors would like to thank E. Montgomery, G. Garbe, J. Presson, A. Heaton, and M. Whorton at NASA Marshall Space Flight Center for their financial and technical support.

References

[1]Wie, B., Murphy, D., Paluszek, M., and Thomas, S., "Robust Attitude Control Systems Design for Solar Sails, Part 1: Propellantless Primary ACS," *Proceedings of AIAA Guidance, Navigation and Control Conference and Exhibit*, No. AIAA-2004-5010, August 2004.

[2]Thomas, S., Paluszek, M., Wie, B., and Murphy, D., "Design and Simulation of Sailcraft Attitude Control Systems

Using the Solar Sail Control Toolbox," *Proceedings of AIAA Guidance, Navigation and Control Conference and Exhibit*, No. AIAA-2004-4890, August 2004.

[3]Bodson, M., Chiasson, J., Novotnak, R., and Rekowski, R., "High-Performance Nonlinear Feedback Control of a Permanent Magnet Stepper Motor," *IEEE Transactions on Control Systems Technology*, Vol. 1, No. 1, March 1994, pp. 5–14.

[4]Wie, B., Thomas, S., Paluszek, M., and Murphy, D., "AOCS Design for a 160-m, 450-kg Sailcraft of the Solar Polar Imager (SPI) Vision Mission," *Proceedings of AIAA Joint Propulsion Conference*, No. AIAA-2005-3928, July 2005.

[5]Murphy, D. M., McEachen, M. E., Macy, B. D., and Gaspar, J. L., "Demonstration of a 20-m Solar Sail System," *Proceedings of 46th Structures, Structural Dynamics, and Materials Conference*, No. AIAA 2005-2126, April 2005.

[6]Wie, B., Murphy, D., Paluszek, M., and Thomas, S., "Robust Attitude Control Systems Design for Solar Sails (Part Two): microPPT-based Backup ACS," *Proceedings of AIAA Guidance, Navigation and Control Conference and Exhibit*, August 2004.

[7]Gawronski, W. K., *Dynamics and Control of Structures*, Springer-Verlag, 1998.